

Probing cosmic ray escape from η Carinae

S. Steinmassl¹, M. Breuhaus¹, R. White¹, B. Reville¹, and J.A. Hinton¹

Max-Planck-Institut für Kernphysik, Postfach 103980, D 69029 Heidelberg, Germany

Accepted 2023-09-06. Received 2023-xx-xx; in original form 2023-xx-xx

ABSTRACT

The binary stellar system η Carinae is one of very few established astrophysical hadron accelerators. It seems likely that at least some fraction of the accelerated particles escape from the system. Copious target material for hadronic interactions and associated γ -ray emission exists on a wide range of spatial scales outside the binary system. This material creates a unique opportunity to trace the propagation of particles into the interstellar medium. Here we analyse γ -ray data from *Fermi*-LAT of η Carinae and surrounding molecular clouds and investigate the many different scales on which escaping particles may interact and produce γ -rays. We find that interactions of escaping cosmic rays from η Carinae in the wind region and the Homunculus Nebula could produce a significant contribution to the γ -ray emission associated with the system. Furthermore, we detect excess emission from the surrounding molecular clouds. The derived radial cosmic-ray excess profile is consistent with a steady injection of cosmic rays by a central source. However, this would require a higher flux of escaping cosmic rays from η Carinae than provided by our model. Therefore it is likely that additional cosmic ray sources contribute to the hadronic γ -ray emission from the clouds.

Key words. radiation mechanisms: non-thermal, gamma rays: stars, stars: winds, outflows, stars: individual: η Carinae, (ISM:)cosmic rays

1. Introduction

Colliding wind binaries (CWBs) are a well-established class of Galactic particle accelerator, with non-thermal emission seen from a number of systems (Moran et al. 1989; Churchwell et al. 1992; Contreras & Rodríguez 1999; Dougherty & Williams 2000; Marcote et al. 2021; del Palacio et al. 2023). In γ -rays, only two systems have been detected so far: η Carinae (e.g. Abdo et al. 2010a) and γ^2 Velorum (Martí-Devesa et al. 2020), located (2.35 ± 0.05) kpc (Smith 2006) and (0.34 ± 0.01) kpc (North et al. 2007) from Earth, respectively. η Carinae (henceforth η Car) is the more luminous of these two systems and has therefore been studied in greater detail. Over its 15-year lifetime, the Fermi Large Area Telescope (LAT) has probed three periastron passages of this highly eccentric ($e \approx 0.9$, Mehner et al. 2015) CWB with an orbital period of ~ 5.5 yr (e.g. Damineli et al. 2008; Teodoro et al. 2016). The high eccentricity and relatively short orbital period, combined with its dense matter and photon fields make η Carinae a unique source in which to study high-energy astrophysical processes in a time-dependent environment.

The Astro-Rivelatore Gamma a Immagini Leggero (AGILE) satellite was used to detect η Car for the first time in γ -rays (Tavani et al. 2009). The detection was soon confirmed by observations with the *Fermi*-LAT satellite (Abdo et al. 2010a; Nolan et al. 2012). Since then, several works have analysed the γ -ray emission measured by *Fermi*-LAT (Abdo et al. 2010b; Farnier et al. 2011; Reitberger et al. 2012, 2015; Balbo & Walter 2017; White et al. 2020; Martí-Devesa & Reimer 2021; Abdollahi et al. 2022a). Two components are apparent in the emitted spectrum above and below ~ 10 GeV (see e.g. Abdo et al. 2010b; Farnier et al. 2011). During the periastron phase when the stars are closest to each other, the emission increases. The peak emission at GeV energies around periastron increases by $\sim 40\%$ relative to the baseline flux (Martí-Devesa & Reimer 2021). Emission up

to 400 GeV has now been established using the High Energy Stereoscopic System (H.E.S.S.) (H. E. S. S. Collaboration et al. 2020).

The γ -ray emission from η Car is generally believed to be emitted by cosmic rays (CRs) accelerated by the shocks that enclose the wind collision region (WCR), where the supersonic winds from the two stars collide to form a pair of standing shocks, separated by a contact discontinuity. The shocks are approximately located at the surface (cap) where the ram pressures from both winds are equal. At the shocks, electrons and protons can be accelerated to relativistic energies and emit γ -rays via synchrotron and inverse Compton processes or via proton-proton collisions with subsequent π^0 -decay, respectively. For the latter process a dense target material is needed to produce a detectable gamma-ray signal. Bednarek & Pabich (2011) were the first to point out that the two shocks in the system should have distinct properties due to the different stellar mass loss rates and terminal wind velocities. These properties result in two different accelerated particle populations. These ideas were developed further by Ohm et al. (2015) and White et al. (2020) (henceforth O15 and W20 respectively) where models were constructed to account for the variable γ -ray emission observed by *Fermi*-LAT and the non-thermal X-ray emission detected with the NuSTAR satellite (Hamaguchi et al. 2018).

In W20, a non-negligible amount of the accelerated protons escape the WCR. Such particles would naturally interact with the surrounding material further out.

The complex environment around η Car provides many potential interaction regions. Though the inner structures, including the binary system and its immediate vicinity, can not be resolved by *Fermi*-LAT or H.E.S.S., the nearby molecular clouds in the Carina Nebula Complex (CNC) and nearby Gum 31 are resolvable. Significant emission associated with these clouds, above

the expectations for the ‘sea’ of diffuse CRs, was reported in W20. Here we explore this emission in more detail.

Recently, Ge et al. (2022) published an analysis of the excess γ -ray emission around η Car considering two Gaussian regions, for which significant emission, likely of hadronic origin was found. They conclude that the emission could be connected to young massive stellar clusters in the region, such as Trumpler 14 and 16. Nevertheless, the authors were not able to rule out, that η Car or yet unknown CR sources are the acceleration sites of the particles producing the γ -ray emission.

In this article, we follow up on these ideas and perform a detailed analysis of the emission from η Car and the surrounding excess emission considering not only two but four different regions. These regions correspond to specific nearby molecular cloud structures connected to the Carina Nebula-Gum 31 complex. Additionally, we analyse possible γ -ray emission from escaping CRs interacting with material on small and large scales around η Car.

While this work focuses primarily on escaping particles accelerated in the WCR, it is also possible that particles have been accelerated in the blast wave from the great eruption of 1843, when the system released more than $10 M_{\odot}$ of material (Smith 2006) with high velocity (Ohm et al. 2010; Skilton et al. 2012). While the apparent orbital variability effectively rules out the possibility that all emission from η Car is due to the blast wave, a significant fraction of the steady emission could still be produced near the blast wave. Though we do not consider them further in this work, these particles would also contribute to the γ -ray emission on larger scales.

The paper is structured as follows: In Section 2, we present an overview of the environment around η Car. This is followed by the analysis of the *Fermi*-LAT data in Section 3. Afterward, we explore possible γ -ray emission from escaping particles on scales not resolvable by *Fermi*-LAT (Section 4) and in the molecular clouds on larger scales (Section 5). In the end, we discuss our findings in Section 6.

2. Environment around η Car

The surroundings in which the η Car binary system is embedded are non-homogeneous with multiple complex structures on a variety of scales. These provide not only a variety of target conditions for CRs escaping from η Car, but also multiple competing sites for particle acceleration. We consider the following zones, in order of increasing scale, as targets for CR interactions and gamma-ray emission:

- **The shock cap/WCR** – the region where the shocks form between the two stars. Following W20 we refer to the more massive star as η Car-A, and the lower mass companion as η Car-B. Depicted as region A in Figure 1.
- **The pinwheel/wind region** – a high-velocity outflow with gradual mixing of the high and low-density winds of the two stars, ending on the scale of the little Homunculus (a possible remnant of an outburst more recent than the great eruption). Depicted as region B in Figure 1.
- **The Homunculus** – the expanding shell associated with the great eruption of 1843. Depicted as region D in Figure 1.
- **The Carina Nebula / Gum 31 complex** – the star formation region containing several massive stellar clusters and 10^3 – 10^5 solar mass molecular clouds (see e.g. Rebolledo et al. 2016). Depicted as region E in Figure 1.

Figure 1 illustrates these different regions graphically. The approximate sizes of these regions are indicated by the coloured

lines below each graphic. Additionally, we illustrate the approximate spatial scales associated with the absorption of the γ -rays. To compute these scales, the stellar parameters were taken to be the same as in W20, but additionally the angular size of the stars was taken into account. While the absorption in W20 was calculated specifically for the emitting region and integrated for specific orbital phase ranges, here we adopted a spherical geometry of the γ -ray emission region for simplicity and the two stars were taken to be at their maximum separation, the apastron position. The black line at the uppermost part of the figure shows the radii for which more than 50 % of γ -rays with an energy of 200 GeV would be absorbed before reaching Earth. The peak absorption occurs close to 600 GeV, and the grey line shows the radial distances inside which more than 10 % of these 600 GeV γ -rays are absorbed. Therefore, accounting for γ -ray absorption is essential for the emission within ~ 200 au of the stars. A detailed plot showing the radial dependence for different energies can be found in Appendix B.

The **shock cap** or **WCR** is formed by the colliding stellar winds. As discussed previously, the winds terminate in a pair of shocks separated by a contact discontinuity. The shock *cap* refers to its finite lateral extent. The global size of this region varies with the orbital phase between ~ 1 au at periastron and ~ 20 au at apastron. At the shocks, particles are expected to be accelerated (see e.g. Eichler & Usov 1993). A detailed discussion of the particle acceleration and emission can be found in O15 and W20.

The shock cap and associated pinwheel are embedded in the **wind region**, which is created by the outflowing winds from both stars. Due to the orbital motion, the winds create a pinwheel like structure, though for η Carinae this is complicated by its eccentric orbit (see Parkin & Pittard 2008). Simulations by Madura et al. (2013) (see also Parkin et al. (2011); Clementel et al. (2014)) find that the fast wind from η Car-B carves out a low-density channel with a large opening angle in the direction of the apastron position. This is a consequence of the brief periastron passage. As is evident in image B in Figure 1, the darker region indicates the low-density wind from η Car-B. Accelerated particles that enter this region experience negligible collisions. On the other hand, any particles that encounter denser wind material from η Car-A within ≈ 100 au from the binary will be collision dominated and have a low probability of escaping the wind region.

The wind region is expected to end as it reaches the **little Homunculus Nebula** (see Figure 1 C). This nebula has a total mass of plausibly $\sim 0.1 M_{\odot}$ (Smith 2005). It is believed to be ejected in the outburst from 1890 and accelerated by the stellar winds. It has a bipolar shape, with the equator being $\sim 2 \times 10^3$ au and the poles around 6.5×10^3 au away from the central stars.

The little Homunculus is in turn embedded in the larger **Homunculus Nebula**, the large bipolar structure shown in image D of Figure 1. The Homunculus was ejected during the great eruption of η Car in the 1840s. It is mainly composed of a thin outer shell, with a thickness of up to 600 au, and a thicker inner shell (Smith 2006). The thin outer shell contains ~ 90 % of the total mass of the Homunculus. The total mass is not exactly known, but it is larger than $10 M_{\odot}$ (Smith et al. 2003) and thought to be between $15 M_{\odot}$ and $35 M_{\odot}$ (Smith & Ferland 2007). This makes the Homunculus the most massive structure in the close proximity of the stars. The equivalent pure atomic hydrogen densities in the thin outer shell are high: at least $3 \times 10^6 \text{ cm}^{-3}$ but potentially 10^7 cm^{-3} or even higher (Smith 2006).

The Homunculus lies within the **Carina Nebula**. As detailed in Rebolledo et al. (2016) (section 5.3), four nearby clouds

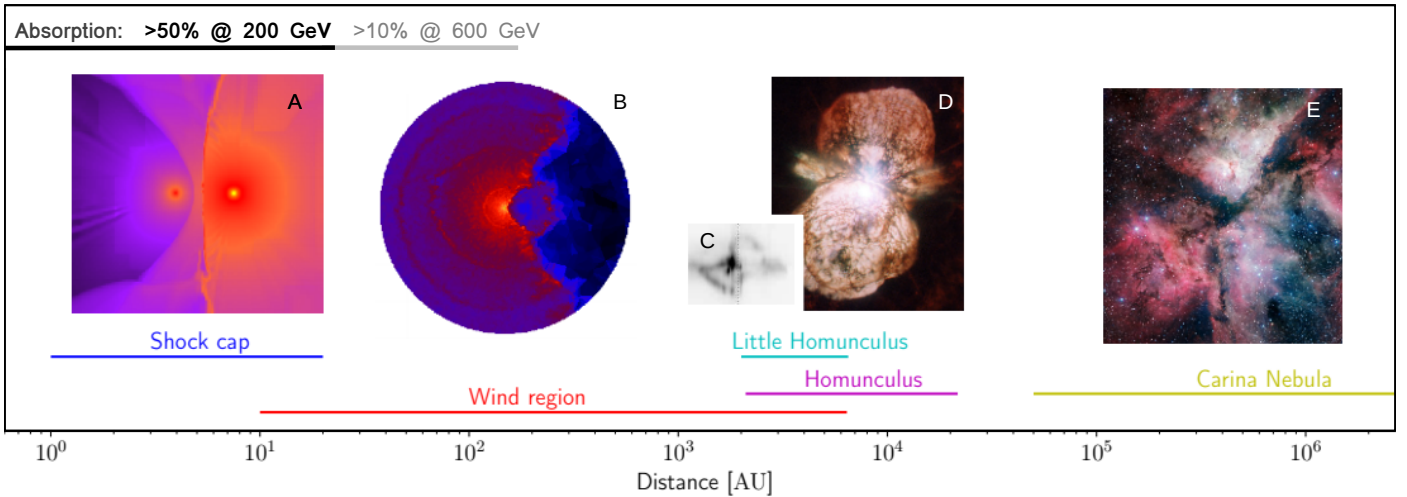


Fig. 1. Scales relevant to the possible emission regions around η Car. Because some regions such as the large or the little Homunculus Nebula are asymmetric, or their size can change over time such as for the shock cap, the sizes shown cover a large range of values. The different extensions are: 1 to 20 au (shock cap, A), 10 to 6.4×10^3 au (wind region, B), 2×10^3 to 6.5×10^3 au (little Homunculus, C), 2.1×10^3 to 21.69×10^3 au (Homunculus, D) and $>50 \times 10^3$ au (Carina Nebula, E). The black and grey bars in the upper left corner indicate the distances beyond which the absorption at 200 GeV is less than 50 % (black) and the absorption at 600 GeV is less than 10 % (grey), see text for more details. The individual images are taken from Parkin et al. (2011), Clementel et al. (2014), Smith (2005), HST, ESO.

with masses of $\approx 10^4$ - $10^5 M_\odot$ are detected in CO maps and also dust measurements. These are referred to as the Southern Cloud, Northern Cloud, Southern Pillars, and Gum 31 and are located within 100 pc of η Car. From the velocity maps presented in that paper, a clear connection to the CNC/Gum 31 complex is evident. Whereas the emission of the binary system down to the scale of the Homunculus is not resolvable with Fermi or H.E.S.S., the larger clouds allow us to probe the CR density around η Car as discussed in Section 3 and Section 5.

3. Fermi analysis and results

The approach to Fermi data analysis here follows closely that of W20. The data selection was based on the latest *Fermi*-LAT Pass 8 data (Briel et al. 2018) starting from Aug 4th, 2008 (MET 239557417) to Oct 26th, 2022 (MET 688521600). Events over an energy range of 500 MeV (chosen to avoid poorly reconstructed events at lower energies) and 500 GeV were included from a region of interest (ROI) of 10° by 10° , centred at the nominal position of η Car and aligned in galactic coordinates. Data were chosen according to the SOURCE event class (*evclass*=128) with FRONT+BACK event types (*evtype*=3). Time periods in which the ROI was observed at zenith angle greater than 90° were excluded. Data were analysed using *Fermitools* (version 2.2.0), which is the official *ScienceTools* suite provided by the Fermi Science Support Center¹ and *FermiPy* (version 1.2) (Wood et al. 2017). The model of sources surrounding η Car was taken similar to W20 and includes all sources in the ROI from the *Fermi*-LAT 12-year source catalog (4FGL-DR3) (Abdollahi et al. 2022b), with the exception of the unidentified point source 4FGL J1046.7-6010, which is located in the centre of the Southern Pillars and was excluded to avoid a potential miss-association of diffuse flux in this region. The model including the diffuse Southern Pillars component instead of the point source 4FGL J1046.7-6010 is preferred by $\Delta TS = 27.3$, whereas adding the point source additionally only improves the model by

$\Delta TS = 7.0$ with 3 additional degrees of freedom. More details on the analysis configuration are summarized in Appendix A.

In W20 an additional diffuse source was added to the model based on the CO survey of Dame et al. (2001). Here, we split the model into four individual clouds, Southern Cloud, Northern Cloud, Southern Pillars and Gum 31, following the region definitions as outlined in Rebolledo et al. (2016) and described in the previous section. The four templates can be seen as an overlay in Figure 2. Each cloud is included in the model as a diffuse component with a power-law spectral shape. Optimisation of the model was performed in an iterative fashion making use of the *optimize* function of *FermiPy*. First, the normalisation of a maximum of 5 of the brightest sources with a predicted number of counts totaling 95% of the total predicted counts of the model are freed and a simultaneous fit is performed. Next, the normalisation of the sources not included in the first step was performed individually. Finally, the shape and normalisation of all sources with a TS exceeding 25 in the previous fits were freed and a simultaneous fit was performed. The same process was repeated but allowing up to ten sources for the first optimization step. After optimising the model, the cloud component spectral shapes were fixed in a first fitting iteration freeing η Car (4FGL J1045.1-5940) and the normalisation of all sources within a 3° radius and with TS values >10 and more than 10 predicted counts. As in the 4FGL catalogue, and previous analysis of the region (W20, Martí-Devesa & Reimer 2021), η Car was modelled as a point source with a log-parabola spectrum $\phi = \phi_0 (E/E_0)^{-\alpha - \beta \log(E/E_0)}$. This yielded a best fit model for η Car with $\alpha = 2.29 \pm 0.02$, $\beta = 0.11 \pm 0.01$, $\phi_0 = (2.44 \pm 0.07) \times 10^{-6} \text{ cm}^{-2} \text{ erg}^{-1} \text{ s}^{-1}$ and $E_0 = 2.11 \text{ GeV}$ consistent with previous studies (W20, Martí-Devesa & Reimer 2021). In a second fitting iteration η Car and all other previously free sources were fixed and the normalisation and spectral shape of all four clouds were freed. Hence any miss-association of flux between the close Southern and Northern Clouds and the bright η Car could be minimised. Following the fitting for η Car and the molecular clouds, a spectral energy distribution (SED) was generated for the source of interest. Whereas a similar event selection approach was taken in

¹ <https://fermi.gsfc.nasa.gov/ssc/>

Cloud Name	Spectral Index	Energy Flux [$\text{erg cm}^{-2} \text{s}^{-1}$]	TS
Southern Cloud	2.30 ± 0.05	$(2.4 \pm 0.3) \times 10^{-11}$	276
Northern Cloud	2.25 ± 0.06	$(2.0 \pm 0.2) \times 10^{-11}$	225
Southern Pillars	2.54 ± 0.06	$(1.8 \pm 0.2) \times 10^{-11}$	348
Gum 31	2.24 ± 0.06	$(2.4 \pm 0.3) \times 10^{-11}$	270

Table 1. TS values and power-law spectral properties of the cloud templates as included in the model and derived by the fit. The energy flux is derived by integrating from 500 MeV to 100 GeV.

Ge et al. (2022), their main result is based on the addition of two Gaussian disks in the fit instead of the cloud templates employed in this work.

The four clouds were each detected with significant excesses and TS values of >200 . The exact values are summarised in Table 1. If a photon weighting procedure as used in the 4FGL catalog (Abdollahi et al. 2020) is applied the TS values are reduced but still >150 for each cloud. The residual emission in the ROI could be clearly reduced with the addition of the cloud templates, as shown in Figure 2. The remaining residual emission to the right side of the region can not be associated with molecular clouds in the CNC/Gum 31 complex (Rebolledo et al. 2016) but might be connected to diffuse emission around West-erlund 2 (Yang et al. 2018). In order to account for it in the fit an additional diffuse component based on the CO map by Dame et al. (2001) was introduced. The inclusion of this additional component helped to improve the overall fit but did not affect the properties of the cloud components significantly. The spectra of the four individual clouds are shown in Figure 3 and the best-fit spectral parameters are also included in Table 1. The spectral results with and without the photon weighting differ only by up to 0.04 for the spectral index and 3% on the energy flux, hence being consistent within the statistical uncertainties. The values without the additional weighting are adopted, whereas the quoted differences can be interpreted as a contribution to the systematic uncertainty. For comparison, the spectrum of η Car is also shown. The spectral shapes and normalisations determined for the Southern Cloud, Northern Cloud and Gum 31 regions show a reasonable level of consistency, with a spectral index between 2.2 and 2.3. In contrast, the Southern Pillars are described by a slightly softer spectrum, mostly caused by an apparent cutoff above photon energies of 20 GeV. Below that energy, the derived flux points are comparable amongst all four clouds. Different spectral models for each cloud were tested by fitting the SEDs of each cloud separately. This yielded a difference of as much as 10% for the integrated energy flux, which can be considered as a contribution to the systematic uncertainty of the analysis.

The inner regions of the Carina Nebula are not resolvable with current γ -ray instruments. For example, the Homunculus exists on scales corresponding to a factor 40 smaller than the 68% containment radius of the Fermi Point Spread Function (PSF), which is $\sim 0.1^\circ$ above 20 GeV (Abdollahi et al. 2020). An upper limit on the γ -ray flux originating from this inner region (but outside the WCR) can hence only be estimated via the quiescent baseline component of the η Car γ -ray flux. Long-term light curves show only mild variability (e.g. W20, Martí-Devesa & Reimer 2021), with the γ -ray flux never dropping below 60% of the mean integrated flux level. This provides a baseline energy flux of $(5.6 \pm 0.3) \times 10^{-11} \text{ erg cm}^{-2} \text{s}^{-1}$ integrated from 500 MeV to 100 GeV.

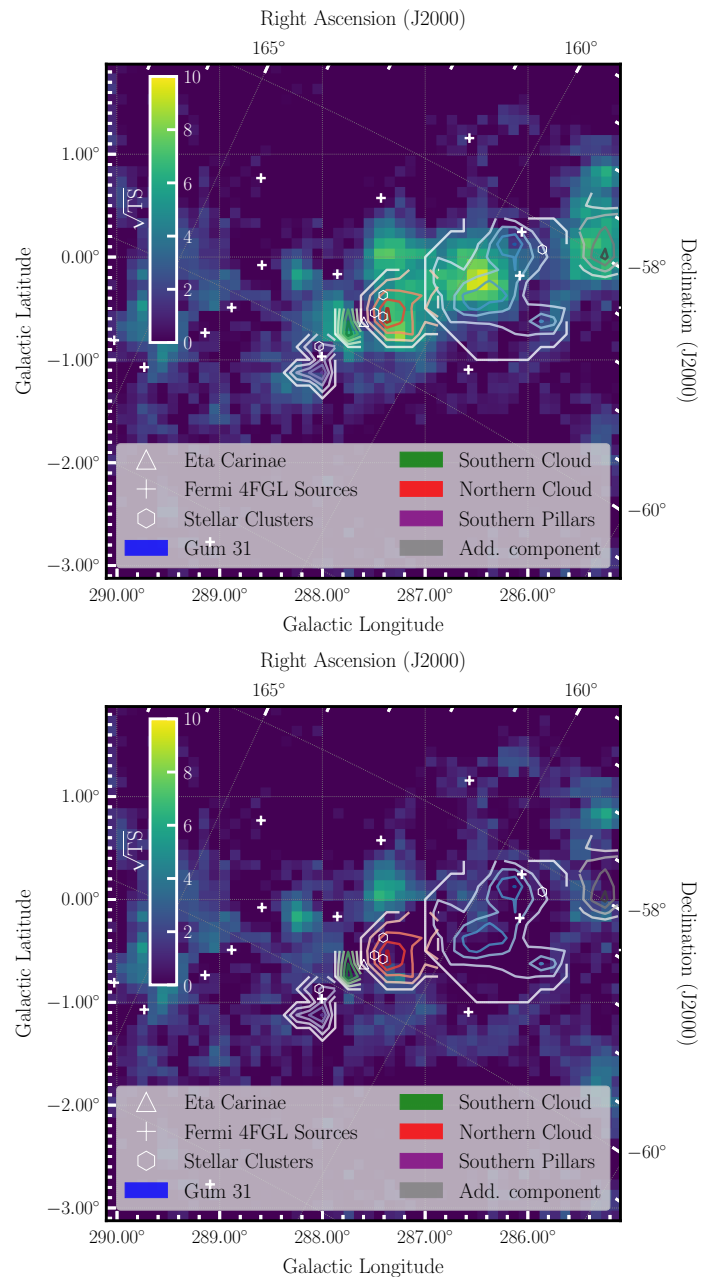


Fig. 2. Residual significance maps from the *Fermi*-LAT analysis in a zoomed region of the ROI. In the upper panel, the $\sqrt{\text{TS}}$ map without the addition of the cloud templates to the model is shown, whereas they are included in the lower panel. In each plot the cloud templates are overlaid by coloured contours, indicating the gas density distribution. Additionally, all other 4FGL sources are marked together with massive stellar clusters from Preibisch et al. (2011).

4. Propagation of CRs around η Car and expected emission

4.1. Particle acceleration and emission in the WCR

We summarise in the following the relevant points of the model of O15, W20 for CR production in the WCR (see also Eichler & Usov 1993; Bednarek & Pabich 2011). The model from W20 is then used to obtain the spectrum of escaping CRs.

As mentioned in Section 2, the WCR contains two shocks. The wind of the more massive star η Car-A is slower (terminal wind speed $v_\infty \approx 5 \times 10^2 \text{ km s}^{-1}$) and more dense

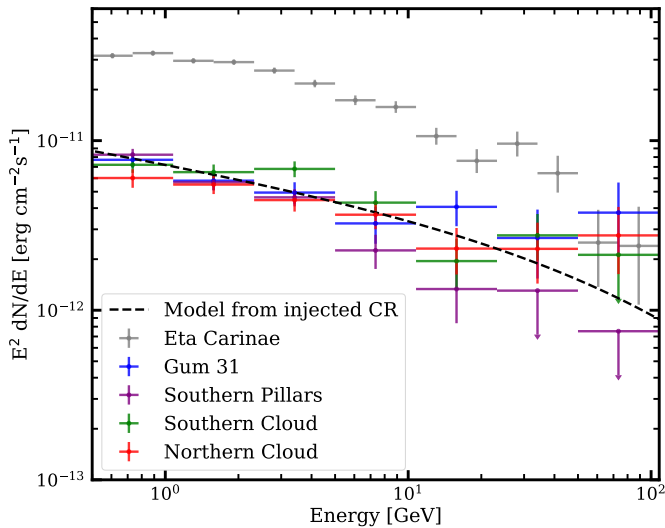


Fig. 3. Spectra of the four molecular clouds as derived from the *Fermi*-LAT analysis. For comparison, the spectrum derived for η Car is also shown in grey. Additionally, a model derived from an injected CR spectrum is shown. The CR spectrum is modeled as a power law with an index of 2.0 and an exponential cutoff at 2 TeV. The normalization has been scaled arbitrarily.

($\dot{M} \approx 4.8 \times 10^{-4} M_{\odot} \text{ yr}^{-1}$) compared to that of the companion star η Car-B ($v_{\infty} \approx 3 \times 10^3 \text{ km s}^{-1}$, $\dot{M} \approx 1.4 \times 10^{-5} M_{\odot} \text{ yr}^{-1}$, see [Parkin et al. 2011](#)). At the side of η Car-A, the high density leads to complete cooling of accelerated protons. The maximum proton energy is limited by inelastic collisions with compressed wind material, with $E_{\text{max}} \sim 200 \text{ GeV}$, and no energetic particles escape the acceleration region. On the side of η Car-B, the cooling time via collisions greatly exceeds the flow time, and accelerated particles can leave the acceleration region. [W20](#) estimated that the maximum proton energy achievable at the wind termination shock of η Car-B is $\approx 30 \text{ TeV}$.

To match observations, approximately 10 % of the wind power processed by each of the shocks should be converted into accelerated protons above 1 GeV. While energetic particles on the side of η Car-A are completely destroyed via hadronic collisions, on the side of η Car-B particles can enter the ballistic region, i.e. the flow transporting the shocked material laterally away from the WCR. The accelerated protons from the shock of η Car-B produce a non-negligible amount of γ -rays in the ballistic region as the shocked material from η Car-B mixes with the shocked higher density material from η Car-A. The amount of radiation produced depends on the details of the mixing process, which was adjusted in [W20](#) to match the *Fermi*-LAT data. The number of interacting particles in the [W20](#) model varies with phase and is largest at periastron.

For γ -rays produced in the wind region close to the stars, absorption due to pair production plays an important role. Here, we restrict ourselves to the assumption of spherically symmetric emission. Due to the change in the stellar positions, there is an orbital variation in the absorption - in particular between phases 0.9 and 0.2. However, for emission on radial distance scales of 20 au, the phase dependence drops below 7 % and decreases rapidly for emission on even larger scales.

In [Figure 1](#) the absorption for spherically symmetric emission at phase 0.5 for two different energies is shown. The case of 600 GeV corresponds roughly to maximum absorption. Whereas at 20 au close to half of the emission is absorbed, at 200 au more

than 90 % of the γ -rays reach Earth. Thus, the VHE γ -ray emission reported by [H. E. S. S. Collaboration et al. \(2020\)](#) can be easier accounted for if it is produced at larger radii.

In the following, we use the average escaping CR spectrum and the stellar wind parameters quoted above, adapted from the model of [W20](#), to investigate possible γ -ray emission produced by the escaping protons in the surrounding environment. Because the escaping proton spectrum in that work was not calculated directly, here it was inferred from the γ -ray data presented in [W20](#). To obtain the spectral shape, we used the Naima package ([Zabalza 2015](#)) assuming an exponential cutoff power-law proton spectrum. In the off-periastron phase range, this resulted in a power-law index of $\alpha \approx 2$ and cutoff energy of $E_{\text{cut}} \approx 1.8 \text{ TeV}$. In [W20](#) the γ -ray spectrum is calculated while the particles are advected with the flow out to a distance where the resulting emission is negligible and the radiative energy losses do not further change the underlying spectrum. The spectrum of escaping particles is then assumed to maintain the same shape. The proton spectrum above 1 GeV was then normalised such that the total energy in escaping protons and transferred into γ rays, secondary particles and directly accelerated electrons is equal to the total power put into particle acceleration. Approximately ~ 90 % of the accelerated protons at the side of η Car B escape from the WCR.

4.2. Propagation in the wind region

The energetic particles that escape in the ballistic flow will eventually merge with the winds. To avoid substantial adiabatic losses, the transport of these particles should be diffusion dominated. The ratio of the characteristic advection and diffusion timescales is a useful measure of which process dominates the radial transport:

$$\frac{t_{\text{adv}}}{t_{\text{diff}}} = \frac{R}{u} \times \frac{D_r}{R^2} = \frac{D_r}{uR} \quad (1)$$

where u is the outward flow speed, D_r the average radial diffusion coefficient, and R the radial distance from the binary. Taking $u \sim 1000 \text{ km s}^{-1}$ and $R = 100 \text{ au}$, adiabatic losses can be neglected provided $D_r \gg 10^{23} \text{ cm}^2 \text{ s}^{-1}$. While the radial diffusion coefficient is not known, the magnetic fields will be highly disordered in the ballistic region provided mixing is effective. This can in principle allow relativistic protons and other nuclei to decouple from the flow and escape the wind region without undergoing significant adiabatic losses.

If, on the other hand, particles were strongly coupled to the flow, the maximum energy would be reduced by adiabatic cooling: $E \propto \rho^{1/3} \propto r^{-2/3}$. Thus in crossing the wind region, the maximum particle energy would be reduced by a factor of 10 or more. If the VHE measurements of [H. E. S. S. Collaboration et al. \(2020\)](#) are produced far from the WCR, this provides a (model-dependent) constraint on the transport.

Protons that move outward, by either diffusion or advection, but remain in the low-density cavity evacuated by the wind from η Car-B, will produce negligible γ -ray emission. However, some protons might migrate into the high-density wind from η Car-A, radiate significantly, and if they remain in the high-density zone, lose all of their energy via hadronic interactions.

The spectrum of the protons migrating into the η Car-A wind will depend on the transport processes, the details of which are currently not well-constrained. In the most extreme case, when all protons penetrate into the wind of η Car-A, the energy in γ rays detected on Earth using a total energy flux in escaping

particles of $6.5 \times 10^{35} \text{ erg s}^{-1}$ from the model of W20 would be $10^{-9} \text{ erg cm}^{-2} \text{ s}^{-1}$. This exceeds considerably the flux detected by *Fermi*-LAT, and the model parameters of W20 would have to be adapted. In the other extreme case, if a transport barrier exists at the interface of the two winds, excluding CRs from the denser target material, no significant emission would be produced in the wind region.

Variability of the γ -ray emission in the wind region are likely to be modest and not necessarily linked to the orbital phase, unless the γ rays are produced only very close to the stars. Any potential emission from escaping protons in the wind region will thus contribute to an approximately steady baseline flux, modulo turbulent variations. The same should hold true for larger structures such as the little and large Homunculus nebulae.

4.3. The little and large Homunculus nebulae

As shown in the previous section, only the particles diffusing in the low-density wind from η Car-B will leave the pinwheel/wind region and in the most extreme case, this could be the vast majority of the particles leaving the WCR. After the wind region, the CRs encounter the little Homunculus Nebula, which is likely to have a total mass of $\sim 0.1 M_{\odot}$ (Smith 2005). On larger scales they encounter the $>10 M_{\odot}$ Homunculus Nebula (see Section 2). To obtain a rough estimate of the total γ -ray emission in each region, we can use the following approximation:

$$F_{\text{Earth}} \approx \frac{t_{\text{cross}}}{t_{\text{cool}}} \cdot \frac{L_{\text{esc}}}{4\pi d^2}, \quad (2)$$

where F_{Earth} is the total energy flux on Earth, t_{cross} the time it takes for the particles to cross each region, t_{cool} the cooling time, L_{esc} the total energy in escaping particles and $d = 2.3 \text{ kpc}$ the distance towards η Car. For L_{esc} we adopt the value of $6.5 \times 10^{35} \text{ erg s}^{-1}$ from the model of W20, assuming that energy losses are negligible in the pinwheel/wind region. We model the little Homunculus and the inner and outer shells of the large Homunculus as spherical shells around the stars for simplicity. We first consider the case of no diffusion within these thin shells, with CRs simply passing through at (close to) the speed of light.

Smith (2005) estimated a thickness of the little Homunculus of $\sim 940 \text{ au}$. Using an average inner radius of $4 \times 10^3 \text{ au}$, a thickness of the shell of 1000 au and a mass of $0.1 M_{\odot}$, the cooling time at 1 GeV is $\sim 4 \times 10^5 \text{ d}$. If the CRs move through the region with the speed of light, the resulting total energy flux on Earth is $F_{\text{Earth}} = 1.4 \times 10^{-14} \text{ erg cm}^{-2} \text{ s}^{-1}$. This is orders of magnitudes below the energy flux from *Fermi*-LAT of $5.6 \times 10^{-11} \text{ erg cm}^{-2} \text{ s}^{-1}$. The inner shell of the large Homunculus contains 10 % of the total Homunculus mass (Smith 2006), which is between $1 M_{\odot}$ and $3.4 M_{\odot}$. To model it as a shell, we assume an inner radius of $1 \times 10^4 \text{ au}$ and an outer radius of $1.5 \times 10^4 \text{ au}$. For a mass of $\sim 2 M_{\odot}$, the resulting F_{Earth} is $3.7 \times 10^{-14} \text{ erg cm}^{-2} \text{ s}^{-1}$. Different values of the inner and outer radius of the shell give similar results. For the outer Homunculus shell with an assumed density of $1.0 \times 10^7 \text{ cm}^{-3}$ and a thickness of 600 au , one obtains $F_{\text{Earth}} = 6.2 \times 10^{-13} \text{ erg cm}^{-2} \text{ s}^{-1}$. The outer Homunculus shell is therefore the most important region for the production of γ rays by the escaping particles with fluxes at least one order of magnitude above the fluxes from the little Homunculus and the inner Homunculus shell. However, if the CRs pass through the outer shell at the speed of light, the γ -ray emission produced is still two orders of magnitude below the *Fermi*-LAT flux.

The Weigelt knots, located closer to the binary, have not been explicitly considered in this study. Adopting the typical Weigelt

knots parameters from Remmen et al. (2013), the knots do not appear to have a sufficiently high over-density relative to the parameters adopted for the Homunculus Nebula to make a significant difference to the gamma-ray luminosity on those scales.

Cosmic rays are more likely to diffuse slowly through these shells of material, than pass through at the speed of light. The outer Homunculus shell is the most massive and the most dense of the three shells, with likely larger magnetic fields and slower diffusion and hence expected to dominate also in this case. We therefore restrict the following calculations for different diffusion coefficients to emission from the outer shell. For simplicity, we ignore possible spectral changes caused by the propagation through the wind region, the little Homunculus and the inner Homunculus shell, because the exact propagation properties are unknown and are impossible to separate observationally from spectral changes by the propagation through the Homunculus itself. As before we adopt a value of $1.0 \times 10^7 \text{ cm}^{-3}$ for the density in the outer shell. A lower limit on the (parallel) diffusion coefficient can be estimated by assuming Bohm diffusion. Unfortunately, the magnetic field in the shell is unknown and difficult to constrain. Values of $100 \mu\text{G}$ or even higher have been proposed (Aitken et al. 1995). To provide some numerical estimates, we take the energy dependence of the radial diffusion coefficient to have the following form:

$$D_r(E) = D_0 \times \left(\frac{E}{1 \text{ GeV}} \right)^{\alpha}. \quad (3)$$

The dotted blue curve in Figure 4 shows the emission produced in the Homunculus for $D_0 = 9 \times 10^{22} \text{ cm}^2 \text{ s}^{-1}$ and $\alpha = 0.5$. As can be seen, interactions in the Homunculus Nebula of escaping CRs could produce a significant amount of steady γ -ray emission. Thus, models in which particle acceleration at the shock of η Car-A is ineffective, for example, due to a low Mach number or a highly oblique magnetic field, can be replaced with models in which the lower energy γ -rays are principally produced in the Homunculus. In Figure 4 the red curve shows the emission produced by particles accelerated at the shock of η Car-B from the model of W20, the dashed red line is without absorption. The black dashed-dotted line shows this emission added to the emission from the Homunculus shown in the blue dashed-dotted curve for $D_0 = 9 \times 10^{21} \text{ cm}^2 \text{ s}^{-1}$, $\alpha = 1$ and a factor of 1.1 more escaping CRs compared to the model of W20. The combined emission reproduces well the *Fermi*-LAT data over the whole energy range. In such a scenario, the weak phase-dependent variability is entirely produced by changes in the emission from η Car-B close to the binary. The assumed diffusion coefficient in the Homunculus is well above the case of Bohm diffusion for a magnetic field of $100 \mu\text{G}$.

The above model for particle acceleration occurring solely at the companion shock together with steady emission from the Homunculus by the escaping CRs can also account for the hard non-thermal X-ray emission. In the model of W20 the hard X-rays, similar to the γ -rays, are dominated by particles accelerated at the shock of η Car-B. Since that model reproduced the variability, we focus here on the phase averaged emission (see also Breuhaus 2022). While the orbital variability in the γ -ray emission shows energy-dependent behaviour that differs between orbits (Balbo & Walter 2017; Martí-Devesa & Reimer 2021), observations are nevertheless consistent with at least $\sim 60\%$ of the emission being produced by a steady-state source. Using the existing γ -ray data, it is difficult to conclude which of these components dominates the quasi-steady emission, e.g. emission produced near the wind termination shock of η Car-A (W20, Balbo

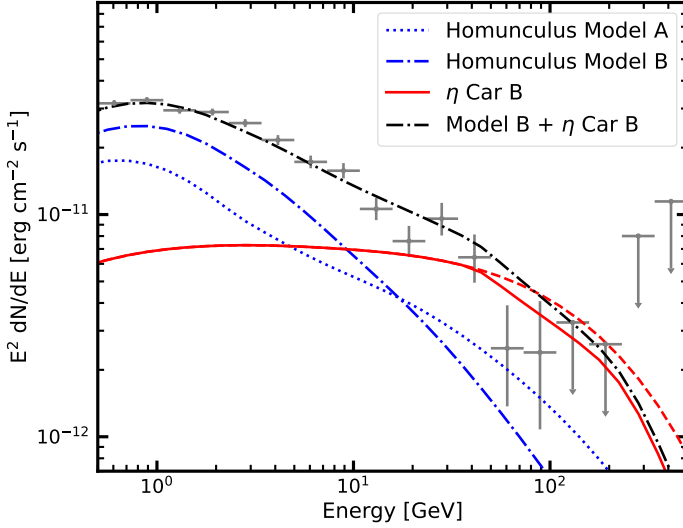


Fig. 4. Model of emission from η Car and the Homunculus together with *Fermi*-LAT data. The blue curves show emission from the Homunculus for different diffusion properties of the escaping CRs. The dotted curve (Model A) is for $D_0 = 9 \times 10^{22} \text{ cm}^2 \text{ s}^{-1}$ and $\alpha = 0.5$. The dashed-dotted curve (Model B) is for $D_0 = 9 \times 10^{21} \text{ cm}^2 \text{ s}^{-1}$, $\alpha = 1$ and a factor of 1.1 more escaping CRs compared to the model from W20. The red solid line shows the emission from η Car produced by particles accelerated at the shock towards η Car B from W20 (the red dashed line is without absorption). The dashed-dotted black curve shows the combined emission from η Car B and Model B.

& Walter 2017), or that produced on larger scales as presented here (see also Ohm et al. 2010; Skilton et al. 2012, for additional large scale sources). An observation of a reduction of the steady part of the emission or a clearly different behavior in different energy bands could potentially constrain the possible contribution of the Homunculus Nebula and the wind region to the gamma-ray flux, though the latter could equally be explained by the turbulent behaviour during the passage as suggested by Martí-Devesa & Reimer (2021).

5. Propagation in the Carina Nebula

CRs that escape both η Car and the Homunculus Nebula will eventually enter the Carina Nebula. There they will encounter the molecular clouds described in Section 2 as potential target material for further γ -ray production. The clouds of the CNC and Gum 31 exhibit significant γ -ray emission (see Section 3) which could be related to η Car. Figure 3 also contains a model γ -ray spectrum derived from an injected CR distribution following a power-law with exponential cutoff. In the models of O15 and W20 a non-linear DSA model was used to account for the required hard underlying proton spectrum (see Section 4.1). The assumed CR spectrum has an index of 2.0 and an exponential cutoff at 2 TeV. To compute a γ -ray spectrum the parametrizations from Kappes et al. (2007) were employed and energy-dependent propagation leading to a softening of $-1/3$ was assumed. The resulting γ -ray spectrum has a similar profile to that measured by *Fermi*-LAT. The CR density in a certain region can be calculated from the γ -ray luminosity and cloud mass following the approximation given in Aharonian et al. (2019):

$$w_{CR}(\geq 10 E_\gamma) = 1.8 \times 10^{-2} \left(\frac{\eta}{1.5} \right)^{-1} \left(\frac{L_\gamma(\geq E_\gamma)}{10^{34} \text{ erg s}^{-1}} \right) \left(\frac{M}{10^6 M_\odot} \right)^{-1} \text{ eV cm}^{-3} \quad (4)$$

Here the parameter η accounts for the presence of heavier nuclei and is assumed to be 1.5. The γ -ray luminosity, L_γ , above 500 MeV is derived from integrating the γ -ray flux and assuming a typical distance of 2.3 kpc, i.e. the same as η Car. This translates to a minimum CR energy of 5 GeV. The masses are assumed to follow the dust mass estimate from Rebolledo et al. (2016), Table 2 based on Herschel infrared Galactic Plane Survey (HiGAL, Molinari et al. 2010) data. The mass uncertainty derived from dust maps is mostly dominated by uncertainties in temperature derivation ($\sim 10\%$) (Urquhart et al. 2018) the HiGAL survey flux ($\sim 5\%$) (Molinari et al. 2016) and the local gas-to-dust mass ratio assumption. According to Giannetti et al. (2017) the local variation of this ratio is of order 20%. Hence we adopt an overall uncertainty of 25% on the mass, not reflecting systematic uncertainties that are common to all of the clouds (which are likely much larger, but do not impact the shape of the profile).

The resulting CR density profile can be seen in Figure 5. The physical extent is visualized by the horizontal error bars as the minimum and maximum distance from η Car. The conversion to a physical distance scale assumes that all clouds are located in a plane at the same distance from the observer. Compared to the result obtained by Ge et al. (2022) the result from Gum 31 is consistent with their result for region B, whereas their region A centred at η Car comprises both the Southern Cloud and parts of the Northern Cloud and is hence not directly comparable.

Assuming η Car as the origin of the CRs, this suggests a $1/r$ profile, similar to that observed around some massive stellar clusters (Aharonian et al. 2019),

$$w_{CR}(r) = w_0 (r/r_0)^{-1}. \quad (5)$$

Normalising the profile at $r_0 = 10$ pc, a value of $w_0 = 0.48 \pm 0.09 \text{ eV cm}^{-3}$ in CRs above 5 GeV is obtained from a fit to the derived CR density profile. Using the maximum energy flux and mass for the Homunculus, as discussed above, provides an upper limit on the CR energy density of $\sim 10^3 \text{ eV cm}^{-3}$ at a distance of $\lesssim 0.1$ pc, which does not constrain the postulated $1/r$ behaviour. For an integration radius of 60 pc, corresponding to the outer edge of the emission seen in the CNC-Gum 31 complex, the derived CR energy density implies a total energy of CR protons of $W_p = 5 \times 10^{48} \text{ erg}$.

The diffusion time can be calculated from the maximum distance, R_{max} , that CRs have propagated for a given diffusion coefficient. Here, R_{max} is taken to be 60 pc and the energy-dependent diffusion is assumed to follow Equation 3. Together with a total power of $\sim 5 \times 10^{35} \text{ erg s}^{-1}$ escaping η Car in CRs above an energy of 5 GeV as suggested by the model in W20, this implies a diffusion coefficient of $D_0 = 5 \times 10^{26} \text{ cm}^2 \text{ s}^{-1}$. Whilst this is slower than the average Galactic diffusion coefficient ($3 \times 10^{28} \text{ cm}^2 \text{ s}^{-1}$), it is well above the lower limit of $5 \times 10^{25} \text{ cm}^2 \text{ s}^{-1}$ implied by the age of η Car ($\sim 2 - 3 \times 10^6$ years (Mehner et al. 2010)), and so, at first sight, may appear reasonable.

However, this diffusion coefficient implies diffusion times through the clouds that are on the same scale as the lifetime of the diffusing protons. The diffusion time through the northern cloud for our estimated diffusion coefficient and a cloud diameter of 30 pc, estimated from the size of the CO template, is $\sim 1.4 \times 10^5 \text{ yr}$. The life time of the diffusing protons is approximately $t_{\text{cool}} = 3 \times 10^7 n^{-1} \text{ yr}$ (e.g. Hinton & Hofmann 2009), corresponding to $\approx 10^5 \text{ yr}$ for a spherical cloud of mass $10^5 M_\odot$ (Rebolledo et al. 2016). Consequently, the thin target approximation does not hold. Faster diffusion appears to be needed, leading to a higher total CR power which can not be produced exclusively from η Car in its current state.

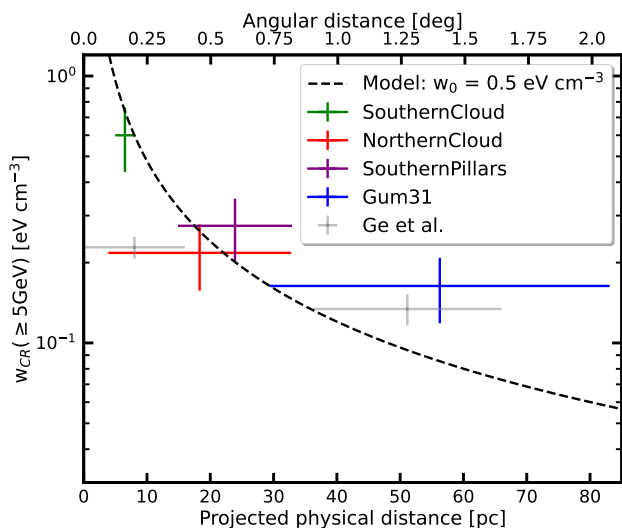


Fig. 5. The CR density for each of the four clouds as a function of distance to η Car. The angular distance has been transformed to a physical using a distance of 2.3 kpc. Distance errors depict the maximum extent of the cloud templates. A $1/r$ type profile as described in Equation 5 has been fit to the data points and is shown by the dashed line. For comparison, the CR densities as derived in Ge et al. (2022) for their regions A & B are shown in light grey.

Therefore either the CR output from η Car was higher in the past by at least a factor of few, or a contribution from additional sources in the CNC is needed. η Car is known to be a highly variable system on timescales of ~ 100 yr, and little is known about the system prior to the great eruption in the 19th century. Equally, several candidate sources exist that could contribute to the observed emission, including massive stellar clusters (such as the nearby Trumpler 14) and massive binaries situated in the star-forming regions of the CNC (Ge et al. 2022; Aharonian et al. 2019).

6. Summary and conclusion

In this work, we analysed *Fermi*-LAT data from η Car and four surrounding clouds and investigated CR escape, propagation and γ -ray emission from the η Car binary system and its neighbourhood. The η Car system and its surroundings are extremely complex, with the wind region, the little and large Homunculus nebulae, and molecular clouds nearby. For efficient escape of particles from the system, the CRs should diffuse in the low-density region carved by the wind from η Car-B, otherwise, they will either interact in the wind region or lose their energy via adiabatic losses. Particles diffusing into the high-density region can lead to an additional contribution to the total γ -ray spectrum. Depending on the propagation properties, the interaction of escaping particles in the Homunculus Nebula can account for a large fraction of the total γ -rays measured by *Fermi*-LAT.

We find that the observed emission of η Car on scales not resolvable by *Fermi*-LAT can be accounted for by a variety of different models. Additionally to that put forward by W20, this also includes models solely accelerating particles at the shock on the side η Car-B, with the lower energy *Fermi*-LAT emission dominantly produced in the Homunculus (see Section 4). Therefore, it is possible that contributions from several zones contribute to the overall emission, a fact which should be included in any future model. However, the determination of the exact amount of

emission produced in each region depends on the details of the CR transport and remains a challenge.

Escaping CRs from η Car may also interact in the molecular clouds of the Carina nebula. As shown in Section 5, the derived radial profile of the CR densities seems to be indicative of an origin of CRs from η Car. However, to account for the current emission associated with molecular clouds, either η Car must have been more powerful in the past, or additional CR sources must be present in the region (as proposed by Ge et al. 2022).

Observations of η Car at several hundreds of GeV and TeV energies by Imaging Atmospheric Cherenkov Telescopes are also of great interest. This part of the spectrum is affected by absorption and potential adiabatic losses. Accurate, potentially time-dependent, observations around periastron, therefore help to investigate the propagation properties close to the stars and to constrain the emission regions. Observations from the H.E.S.S. telescopes of the most recent periastron passage, and observations from the future CTA Observatory, may provide crucial information to help unravel the physics of this fascinating binary system η Car.

7. Acknowledgements

For the numerical calculations in Section 4 we made use of the open-source code GAMERA (Hahn 2015; Hahn et al. 2022). To estimate the shape of the escaping proton spectrum, the Naima package was used (Zabalza 2015).

References

- Abdo, A. A., Ackermann, M., Ajello, M., et al. 2010a, *ApJS*, 188, 405
- Abdo, A. A., Ackermann, M., Ajello, M., et al. 2010b, *ApJ*, 723, 649
- Abdollahi, S., Acero, F., Ackermann, M., et al. 2020, *The Astrophysical Journal Supplement Series*, 247, 33
- Abdollahi, S., Acero, F., Ackermann, M., et al. 2022a, *ApJ*, 933, 204
- Abdollahi, S., Acero, F., Baldini, L., et al. 2022b, *ApJS*, 260, 53
- Aharonian, F., Yang, R., & de Oña Wilhelmi, E. 2019, *Nature Astronomy*, 3, 561
- Aitken, D. K., Smith, C. H., Moore, T. J. T., & Roche, P. F. 1995, *MNRAS*, 273, 359
- Aydi, E., Sokolovsky, K. V., Chomiuk, L., et al. 2020, *Nature Astronomy*, 4, 776
- Balbo, M. & Walter, R. 2017, *A&A*, 603, A111
- Bednarek, W. & Pabich, J. 2011, *A&A*, 530, A49
- Breuhaus, M. 2022, dissertation, Ruprecht-Karls-Universität Heidelberg
- Bruel, P., Burnett, T. H., Digel, S. W., et al. 2018, *arXiv e-prints*, arXiv:1810.11394
- Churchwell, E., Biegging, J. H., van der Hucht, K. A., et al. 1992, *ApJ*, 393, 329
- Clementel, N., Madura, T. I., Kruip, C. J. H., Icke, V., & Gull, T. R. 2014, *MNRAS*, 443, 2475
- Contreras, M. E. & Rodríguez, L. F. 1999, *ApJ*, 515, 762
- Dame, T. M., Hartmann, D., & Thaddeus, P. 2001, *ApJ*, 547, 792
- Damineli, A., Hillier, D. J., Corcoran, M. F., et al. 2008, *MNRAS*, 384, 1649
- del Palacio, S., García, F., De Becker, M., et al. 2023, *arXiv e-prints*, arXiv:2302.08170
- Dougherty, S. M. & Williams, P. M. 2000, *MNRAS*, 319, 1005
- Eichler, D. & Usov, V. 1993, *ApJ*, 402, 271
- Farnier, C., Walter, R., & Leyder, J. 2011, *A&A*, 526, A57+
- Ge, T.-T., Sun, X.-N., Yang, R.-Z., Liang, Y.-F., & Liang, E.-W. 2022, *MNRAS*, 517, 5121
- Giannetti, A., Leurini, S., König, C., et al. 2017, *A&A*, 606, L12
- Gould, R. J. & Schröder, G. P. 1967, *Phys. Rev.*, 155, 1404
- H. E. S. S. Collaboration, Abdalla, H., Adam, R., et al. 2020, *A&A*, 635, A167
- Hahn, J. 2015, in *International Cosmic Ray Conference*, Vol. 34, 34th International Cosmic Ray Conference (ICRC2015), 917
- Hahn, J., Romoli, C., & Breuhaus, M. 2022, *GAMERA: Source modeling in gamma astronomy*, Astrophysics Source Code Library, record ascl:2203.007
- Hamaguchi, K., Corcoran, M. F., Pittard, J. M., et al. 2018, *Nature Astronomy*, 2, 731
- Hillier, D. J., Davidson, K., Ishibashi, K., & Gull, T. 2001, *ApJ*, 553, 837
- Hinton, J. A. & Hofmann, W. 2009, *ARA&A*, 47, 523
- Kappes, A., Hinton, J., Stegmann, C., & Aharonian, F. A. 2007, *ApJ*, 656, 870
- Madura, T. I., Gull, T. R., Okazaki, A. T., et al. 2013, *MNRAS*, 436, 3820
- Madura, T. I., Gull, T. R., Owocki, S. P., et al. 2012, *MNRAS*, 420, 2064

- Marcote, B., Callingham, J. R., De Becker, M., et al. 2021, *MNRAS*, 501, 2478
- Martí-Devesa, G. & Reimer, O. 2021, *A&A*, 654, A44
- Martí-Devesa, G., Reimer, O., Li, J., & Torres, D. F. 2020, *A&A*, 635, A141
- Mehner, A., Davidson, K., Ferland, G. J., & Humphreys, R. M. 2010, *ApJ*, 710, 729
- Mehner, A., Davidson, K., Humphreys, R. M., et al. 2015, *A&A*, 578, A122
- Molinari, S., Schisano, E., Elia, D., et al. 2016, *A&A*, 591, A149
- Molinari, S., Swinyard, B., Bally, J., et al. 2010, *PASP*, 122, 314
- Moran, J. P., Davis, R. J., Bode, M. F., et al. 1989, *Nature*, 340, 449
- Nolan, P. L., Abdo, A. A., Ackermann, M., et al. 2012, *ApJS*, 199, 31
- North, J. R., Tuthill, P. G., Tango, W. J., & Davis, J. 2007, *MNRAS*, 377, 415
- Ohm, S., Hinton, J. A., & Domainko, W. 2010, *ApJ*, 718, L161
- Ohm, S., Zabalza, V., Hinton, J. A., & Parkin, E. R. 2015, *MNRAS*, 449, L132
- Parkin, E. R. & Pittard, J. M. 2008, *MNRAS*, 388, 1047
- Parkin, E. R., Pittard, J. M., Corcoran, M. F., & Hamaguchi, K. 2011, *ApJ*, 726, 105
- Preibisch, T., Ratzka, T., Kuderna, B., et al. 2011, *A&A*, 530, A34
- Rebolledo, D., Burton, M., Green, A., et al. 2016, *MNRAS*, 456, 2406
- Reitberger, K., Reimer, A., Reimer, O., & Takahashi, H. 2015, *A&A*, 577, A100
- Reitberger, K., Reimer, O., Reimer, A., et al. 2012, *A&A*, 544, A98
- Remmen, G. N., Davidson, K., & Mehner, A. 2013, *ApJ*, 773, 27
- Skilton, J. L., Domainko, W., Hinton, J. A., et al. 2012, *A&A*, 539, A101
- Smith, N. 2005, *MNRAS*, 357, 1330
- Smith, N. 2006, *The Astrophysical Journal*, 644, 1151
- Smith, N. & Ferland, G. J. 2007, *The Astrophysical Journal*, 655, 911
- Smith, N., Gehrz, R. D., Hinz, P. M., et al. 2003, *AJ*, 125, 1458
- Tavani, M., Sabatini, S., Pian, E., et al. 2009, *ApJ*, 698, L142
- Teodoro, M., Damineli, A., Heathcote, B., et al. 2016, *ApJ*, 819, 131
- Urquhart, J. S., König, C., Giannetti, A., et al. 2018, *MNRAS*, 473, 1059
- Vernetto, S. & Lipari, P. 2016, *Phys. Rev. D*, 94, 063009
- White, R., Breuhaus, M., Konno, R., et al. 2020, *A&A*, 635, A144
- Wood, M., Caputo, R., Charles, E., et al. 2017, *Proc. of International Cosmic Ray Conference*, 301, 824
- Yang, R.-z., de Oña Wilhelmi, E., & Aharonian, F. 2018, *A&A*, 611, A77
- Zabalza, V. 2015, *Proc. of International Cosmic Ray Conference*, 34, 922

Appendix A: Further *Fermi*-LAT analysis details

Parameter	Value
Data release	P8R3
IRFs	P8R3_SOURCE_V3
ROI data width	10°
ROI model width	15°
Bin size	0.1°
zmax	90°
Coordinate system	GAL
Minimum energy	500 MeV
Maximum Energy	500 GeV
MET start	239557417
MET stop	688521600
MET excluded (ASASSN-18fv)	542144904 – 550885992
evclass	128
evtype	3
edisp	True
edisp binning	-1
edisp disabled	Isotropic and diffuse ²
Galactic diffuse template	gll_iem_v07.fits
Isotropic background component	iso_P8R3_SOURCE_V3_v1.txt
<i>Fermi</i> -LAT catalogue	4FGL-DR3 (gll_psc_v29.fit)

Table A.1. Configuration used for the *Fermi*-LAT analysis. The time period MET 542144904 – 550885992 was excluded due to the bright nova ASASSN-18fv (or V906 Carinae) (Aydi et al. 2020) within the ROI

Appendix B: $\gamma\gamma$ -absorption

For the calculations of $\gamma\gamma$ -absorption in the anisotropic stellar radiation fields, we used the open-source GAMERA code (Hahn 2015; Hahn et al. 2022). It uses the standard cross-section for pair production which can be found, for example, in Gould & Schröder (1967). In the form found for example in Vernetto & Lipari (2016, Eq. 1), the cross-section reads:

$$\sigma_{\gamma\gamma} = \sigma_T \frac{3}{16} (1 - \beta^2) \left[2\beta(\beta^2 - 2) + (3 - \beta^4) \ln \frac{1 + \beta}{1 - \beta} \right], \quad (\text{B.1})$$

where $\beta = \sqrt{1 - 1/x}$ with $x = s/(4m_e^2 c^4)$ and $s = 2E_\gamma \epsilon (1 - \cos \theta)$ the square of the centre-of-mass energy. Here θ is the angle between the propagation directions of the two interacting photons, E_γ the energy of the γ -ray photon, ϵ the energy of the target photon and m_e the electron rest mass.

The propagation direction of the γ -ray photon is towards the observer and the direction of the target photon depends on the position of the stars inferred from the orbital parameters. The eccentricity of the system was assumed to be 0.9 (Damineli et al. 2008), the semi-major axis 16.64 au (Hillier et al. 2001), the inclination of the orbit $i = 135^\circ$ and the position angle $\phi = 10^\circ$ (Madura et al. 2012). For each star, modelled as a black body, Equation B.1 is integrated over the stellar surface, which is assumed to produce photons uniformly. This means that each point of the stellar surface produces the same amount of photons at the

same temperature. The stellar temperatures are the same as in O15 and W20, 2.58×10^4 K for the primary star and 3×10^4 K for the companion.

Figure B.1 shows the transmissivity at 220 GeV, 620 GeV and 4 TeV for different distances from the centre of mass of the system assuming a spherical uniform γ -ray production. As can be seen, the transmissivity increases with increasing radius as expected due to the decreased radiation energy density at larger distances from the stars.

While at a distance of 25 au, the transmissivity at 220 GeV is larger than at 620 GeV, the opposite is the case for distances above ~ 75 au. This is caused by the relative position of the two stars and their different temperatures. η Car B is hotter than η Car A and therefore is more important at lower energies than at higher energies. The relative absorption from each star changes with different radii because of the stellar separation, which is slightly more than 30 au, and because the centre of mass of the system is around five times more distant from η Car B than from η Car A. The relative absorption by target photons from η Car B compared to η Car A increases with distance for the apastron position creating the observed effect for the curves at 220 GeV and 620 GeV.

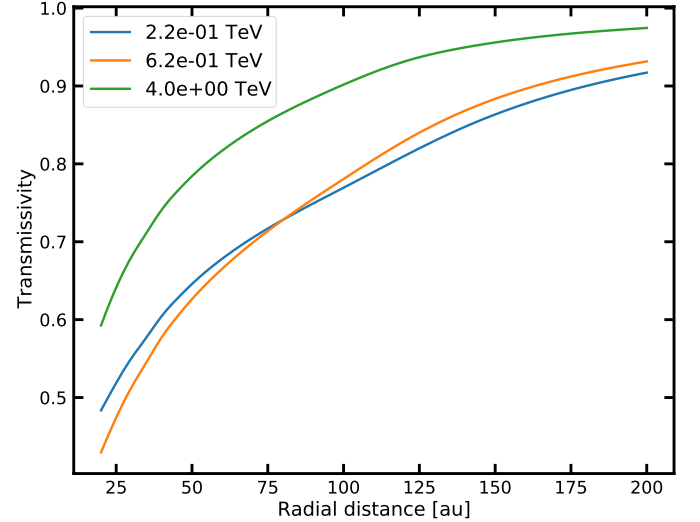


Fig. B.1. Transmissivity versus distance from the centre of mass of the binary system for spherical emission and different energies at an orbital phase of 0.5.

² Even though disabling energy dispersion for the galactic diffuse component is not the standard procedure with a model based on the 4FGL catalog, this does not affect the result significantly due to the high energy threshold of the analysis.